Excellent Sun-Light-Driven Photocatalytic Activity by Aurivillius Layered Perovskites, $Bi_{5-x}La_xTi_3FeO_{15}$ (x = 1, 2)

Gollapally Naresh and Tapas Kumar Mandal*

Department of Chemistry, Indian Institute of Technology Roorkee, Roorkee 247 667, India

S *Supporting Information*

ABSTRACT: Aurivillius phase layered perovskites, $Bi_{5-x}La_xTi_3FeO_{15}$ (x = 1, 2) are synthesized by solid-state reaction. The compounds are characterized by powder X-ray diffraction (PXD), field-emission scanning electron microscopy (FE-SEM), energy-dispersive X-ray spectroscopy (EDS), UV−vis diffuse reflectance (UV−vis DRS), and photoluminescence (PL) spectroscopy. UV−vis DRS data revealed that the compounds are visible light absorbing semiconductors with band gaps ranging from ∼2.0−2.7 eV. Photocatalytic activity studies by Rhodamine B (RhB) degradation under sun-light irradiation showed that these layered oxides are very efficient photocatalysts in mild acidic medium. Scavenger test studies demonstrated that the photogenerated holes and superoxide radicals ($O_2^{•−}$) are the active species responsible for RhB degradation over the Aurivillius layered perovskites. Comparison of PL intensity, dye adsorption and ζ-potential suggested that a slow $e^−$−h^+ recombination and effective dye adsorption are crucial for the degradation process over these photocatalysts. Moreover, relative positioning of the valence and conduction band edges of the semiconductors, $O_2/O_2^{•−}$, $^•OH/H_2O$ potential and HOMO−LUMO levels of RhB appears to be responsible for making the degradation hole-specific. Photocatalytic cycle tests indicated high stability of the catalysts in the reaction medium without any observable loss of activity. This work shows great potential in developing novel photocatalysts with layered structures for sun-light-driven oxidation and degradation processes largely driven by holes and without any intervention of hydroxyl radicals, which is one of the most common reactive oxygen species (ROS) in many advanced oxidation processes.

KEYWORDS: $Bi_{5-x}La_xTi_3FeO_{15}$ (x = 1, 2), layered perovskites, Aurivillius phases, photocatalysis, rhodamine B
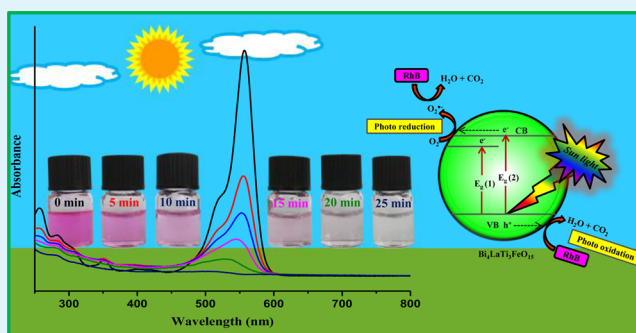
INTRODUCTION

Conversion of solar energy into clean hydrogen energy by water splitting reaction and degradation of organic and inorganic pollutants by visible-light photocatalysis are of immense interest for their potential applications in renewable energy and environmental remediation.[1−4] Photocatalysts based on transition metal oxides working under UV-irradiation have been extensively investigated.[1−4] However, considering the abundance of sun-light in the visible region (accounting for about 43% of incoming solar energy), the development of visible-light-photocatalysts is in demand for efficient utilization of solar energy.

Rhodamine B (RhB) is one of the xanthene dyes which are used in textile industry as coloring agent and in biology as a staining fluorescent dye. During its natural anaerobic degradation, RhB produces aromatic amines that are potentially toxic and carcinogenic. Therefore, photocatalytic degradation and removal of RhB from industrial wastewater is important from health and environmental perspectives.

In recent years, there has been tremendous research thrust in harvesting solar energy by visible-light-driven photocatalysis utilizing single-phase bulk and nanostructured metal oxides.[5−9] Among them, perovskites constitute a major class both with

two- (layered type) and three-dimensional structures.[6−8] It is observed that many oxides studied for visible-light photocatalysis contain Bi^{3+}.[5,6,10−18] The presence of Bi plays a crucial dual role in these materials. First, it pushes the absorption band edge in the visible region because of the formation of a hybridized valence band comprising of Bi 6s and O 2p states[10] and second, the dispersed valence band facilitates oxidation reaction because of high mobility of photogenerated holes.[5,6,19]

Among the Bi^{3+} containing compounds that exhibit visible-light-driven photocatalytic activity, the Aurivillius phases are noteworthy.[12−15,17,18] The Aurivillius phases are variants of layered perovskites where the layered structure is formed by alternating stacks of perovskite slabs, with a general composition $[A_{n-1}B_nO_{3n+1}]^{2−}$ (where n represents n-octahedra thick perovskite block), and the fluorite-like $[Bi_2O_2]^{2+}$ units (Figure 1).[20] Preparation and photocatalytic activities of single-layer (n = 1) Aurivillius type perovskite oxides, such as Bi_2MoO_6,[21,22] Bi_2WO_6,[12,14,23] and their solid solution[24,25] phases have also been investigated. Recently, the four layer (n

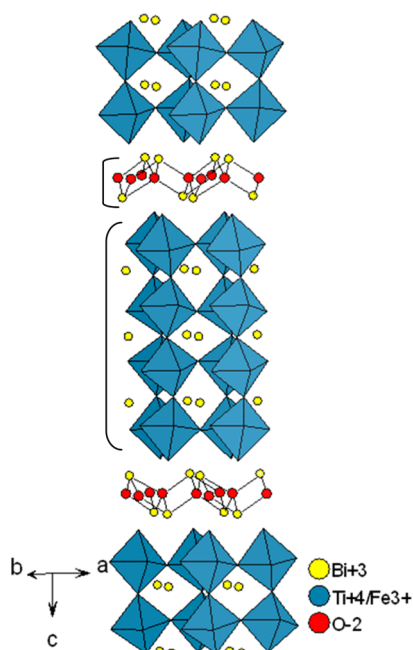**Figure 1.** Structure of four layer ($n = 4$) Aurivillius layered perovskite, $Bi_5Ti_3FeO_{15}$ showing alternate stacks of $[Bi_2O_2]^{2+}$ and $[Bi_3Ti_3FeO_{13}]^{2-}$.

= 4) Aurivillius phase, $Bi_5Ti_3FeO_{15}$, has drawn attention for its ferroelectric[26,27] and photocatalytic[15,17] properties. Photocatalytic activity of $Bi_5Ti_3FeO_{15}$ toward RhB,[15] acetaldehyde[15] and isopropyl alcohol[17] degradation by visible-light irradiation has been reported, although very poor degradation (∼6%) efficiencies were observed with the bulk $Bi_5Ti_3FeO_{15}$ in neutral aqueous solution. However, Sun et al. have shown enhanced RhB degradation with $Bi_5Ti_3FeO_{15}$ hierarchical microflowers as compared to the bulk oxide under similar conditions. The higher efficiency has been attributed to increased surface area and its nanocrystalline nature.[15] Synthesis of $Bi_4LaTi_3FeO_{15}$ by a molten-salt flux method was reported, but the structural parameters and photocatalytic activities are not known.[28] We undertook a systematic exploration on the solid state synthesis and characterization of four layer Aurivillius perovskites, $Bi_{5-x}La_xTi_3FeO_{15}$ ($x = 1$–3). We report here for the first time, to the best of our knowledge, the solid-state synthesis and characterization of $Bi_{5-x}La_xTi_3FeO_{15}$ ($x = 1, 2$). Besides, the effectiveness of bulk photocatalysts toward RhB degradation under sun-light irradiation at different solution pH and their photostability on recycling are reported here in comparison with parent $Bi_5Ti_3FeO_{15}$ bulk oxides. The details of synthesis and characterization of the Aurivillius perovskites, $Bi_{5-x}La_xTi_3FeO_{15}$ ($x = 1, 2$), and mechanistic insight into the sun-light-driven RhB degradation over these catalysts are described.

■ EXPERIMENTAL SECTION

Synthesis. The compounds, $Bi_{5-x}La_xTi_3FeO_{15}$ ($x = 1, 2$), were synthesized by solid-state reactions. For this purpose, stoichiometric quantities of Bi_2O_3 (Sigma-Aldrich, ≥ 98.0%), La_2O_3 (Sigma-Aldrich, 99.99%), (preheated at 950 °C), TiO_2 (Sigma-Aldrich, 99.8%) and $FeC_2O_4\cdot 2H_2O$ were ground thoroughly in an agate mortar for 1h and the powder mixture was heated at 900 °C for 12h followed by 1000 °C for 6h with intermittent grinding. $FeC_2O_4\cdot 2H_2O$ was prepared by precipitation method in aqueous medium by mixing equimolar quantities of $FeCl_2\cdot 4H_2O$ (Sigma-Aldrich, ≥ 99.0%) and oxalic acid

(Merck ≥99.0%). $Bi_5Ti_3FeO_{15}$ was synthesized by a solid-state reaction method, starting with a stoichiometric mixture of Bi_2O_3, TiO_2, and $FeC_2O_4\cdot 2H_2O$, similar to that reported in the literature.[29]

Characterization. *Powder X-ray Diffraction (PXD).* PXD measurements were carried out using a Bruker AXS D8 Advance diffractometer operating at 40 kV and 30 mA with graphite monochromatized CuK_α (1.5406 Å) radiation in the angular range 5−90°. Indexing of the PXD patterns and least-squares refinement of lattice parameters were carried out using the PROSZKI program.[30] PXD pattern simulations were carried out using the POWDERCELL program[31] with slight adjustments to the positional parameters. The positional parameters were generated by multiplying with appropriate factors obtained from the least-squares refined lattice parameter of the compounds and Rietveld refined lattice parameters of the parent $Bi_5Ti_3FeO_{15}$.[32]

Field-Emission Scanning Electron Microscopy (FE-SEM). Morphological studies of the samples were investigated with the aid of a Zeiss FE-SEM, Ultra plus55, operating at an accelerating voltage of 20 kV. The samples were smeared on a carbon tape pasted on an Aluminum stub and coated with a thin layer of Au for electrical conductivity. The elemental compositions and elemental mapping of all the compounds were determined by energy-dispersive X-ray spectroscopy (EDS). Spot and area analyses were carried out to find the elemental compositions in several regions of the samples.

UV−Visible Diffuse Reflectance Spectra (UV−Vis DRS). UV−vis DRS of the as prepared compounds were recorded using a Shimadzu UV-2450 UV−vis spectrophotometer within the wavelength range 200−800 nm. $BaSO_4$ was used as a reference material for baseline correction. The reflectance data were converted to absorption according to the Kubelka−Munk (K-M) theory:[33]

$$F(R_\infty) = (1 - R_\infty)^2/2R_\infty \tag{1}$$

where R_∞ is reflectance of the sample and $F(R_\infty)$ is the K-M function. The band gap of the samples was estimated by Tauc plot. For this, the following expression given by Tauc was used.[34]

$$(\alpha h\nu)^{1/n} = A(h\nu - E_g) \tag{2}$$

where α, $h\nu$, A, and E_g are the absorption coefficient, incident light frequency, proportionality constant and band gap, respectively. The value of exponent, n determines the nature of electronic transition; for assigning direct transition, $n = 1/2$ and for indirect transition, $n = 2$ were used.[35] The linear extrapolation of $(\alpha h\nu)^{1/n}$ to zero gave the band gap energies of the samples.

Photoluminescence (PL) Spectra. PL measurements were carried out on Shimadzu RF-5301PC specrtofluorophotometer at room temperature. The sample for PL study was prepared by dispersing ∼10 mg of solid sample in 10 mL of methanol and sonicating the resulting suspension for 10 min. An excitation wavelength of 350 nm was used to record the spectra.

PL measurements to detect hydroxyl radical (•OH) generation for the present photocatalyst system under sun-light irradiation were carried out using terephthalic acid (TA) as a probe molecule. For this, 0.1 g of $Bi_4LaTi_3FeO_{15}$ powder was dispersed in 100 mL of 5×10^{-4} M aqueous TA solution in alkaline medium (2×10^{-3} M in NaOH). The resulting catalyst-TA suspension was magnetically stirred in the dark for 60 min and then it was exposed to the sun light. At regular time intervals, 5 mL of suspension was taken out and centrifuged to remove the catalyst particles. Then the PL intensity of filtrates was measured by a fluorescence spectrophotometer at an excitation wavelength of 315 nm.

ζ-Potential Measurements. The surface charge of the photocatalyst particles were measured via ζ-potential measurements using Malvern Zeta Sizer Nano ZS90. The experiments were carried out by dispersing 10 mg of solid catalyst in 10 mL of aqueous solutions of different pH (2, 3, 5, 7, 9, 11, and 14). The pH of the solutions was adjusted by adding dilute hydrochloric acid or sodium hydroxide. The catalyst suspensions were sonicated for 10 min prior to each measurements.

Dye Adsorption Studies. To determine the adsorption of RhB on the catalyst surface at different pH, the catalyst suspensions in RhB

solution were magnetically stirred in the dark for 6 h. The initial and final dye concentrations were measured by absorption experiments carried out with a Shimadzu UV-2450 UV−vis spectrophotometer. The percentage adsorption was calculated from the difference between the final and initial dye concentrations.

Photocatalytic Activity Test. Photocatalytic activities of the as prepared compounds were tested by Rhodamine-B (RhB) degradation under natural sun light at different pH. For this, The RhB solution was prepared in aqueous medium and the required pH (2, 3, 7, and 11) of the solutions was adjusted by addition of dilute hydrochloric acid or sodium hydroxide. The degradation experiments were carried out at IIT Roorkee (29°51′ N; 77°53′ E) under similar conditions in the month of February, 2014 (having solar Direct Normal Irradiance ∼187 W/m^2 during the month). In a typical degradation study, 0.1 g of powder photocatalyst was added into 100 mL of RhB solution (1 × 10^{-5} M) of appropriate pH taken in a 250 mL beaker. Then, the dye-catalyst suspensions were magnetically stirred at 350 rpm for 60 min in the dark to ensure adsorption−desorption equilibrium between the photocatalyst and RhB. After this, the beaker containing dye-catalyst suspension was exposed to the direct sun-light irradiation. For measuring dye concentration during the degradation experiments, 5 mL of suspension were sampled at regular time intervals, centrifuged at 8500 rpm to remove the catalyst particles and absorption measurements were carried out with the filtrates using a Shimadzu 2450 UV−visible spectrophotometer. After recording the absorbance at each time interval, the dye solution was put back into the beaker to maintain the constant volume of dye solution so that the errors due to loss of RhB and catalysts are minimized. A blank test was also performed with the RhB solution of same concentration without the catalyst under sun-light irradiation for self-degradation correction and calculation of degradation efficiency. The photocatalytic degradation efficiencies of the catalysts were calculated using the following expression

$$\text{degradation (\%)} = (1 - C/C_0)100 \tag{3}$$

where C_0 is the initial dye concentration and C is the concentration of the dye at different time intervals.

Catalyst Stability and Photocatalytic Cycle Test. The stability of the catalyst in the acidic medium on photocatalytic RhB degradation was investigated by carrying out several cycles of photodegradation with the same catalyst and recording its PXD pattern. For this, a fixed quantity of catalyst (0.1 g) were taken in 100 mL of 1 × 10^{-5} M RhB solution and the photocatalytic degradation studies were performed by the same procedure as mentioned in the activity test. For cycle studies, the catalyst was separated by centrifuging it after the first cycle and recovered from the centrifuge tube into a beaker with the help of a fresh 100 mL of 1 × 10^{-5} M RhB solution. Then, the dye-catalyst suspension was subjected to magnetic stirring for 60 min in the dark and subsequently exposed to the direct sun-light irradiation for the second cycle test. The same procedure was repeated for other cyclic runs and at the end of the fifth cycle, the catalyst was separated, dried and subjected to PXD studies.

Detection of Reactive Species. To investigate the active species responsible for photodegradation, different scavenger tests were carried out. For this purpose, an appropriate scavenger was added to the catalyst-dye suspension and the photodegradation experiment was carried out in the same way as mentioned in the activity test. In our experiments, ethylenediaminetetraacetic acid (EDTA, 1 mM), isopropyl alcohol (IPA, 1 mM) and Ar gas purging was employed as hole (h$^+$),[36] •OH,[37] and O$_2$•$^−$ scavenger, respectively. For scavenger tests, 29.3 mg of solid EDTA and 77 µL of IPA were used for 100 mL of dye-catalyst suspension to make the required concentration of the scavenger as mentioned above.

Chemical Oxygen Demand (COD) Test. COD of the RhB solution before, during and after the photocatalysis was analyzed by using a digestion unit (DRB 200, HACH, USA) and UV−visible spectrophotometer. The following expression was used to calculate the photocatalytic degradation efficiency.

$$\text{potodegradation efficiency} = \left(\frac{\text{initial COD} - \text{final COD}}{\text{initial COD}} \right)100 \tag{4}$$

■ RESULTS AND DISCUSSION

PXD Analysis. The PXD patterns of the as prepared compounds, Bi$_{5-x}$La$_x$Ti$_3$FeO$_{15}$ ($x = 0−2$) are shown in Figure 2. A comparison of the observed PXD data with that of the
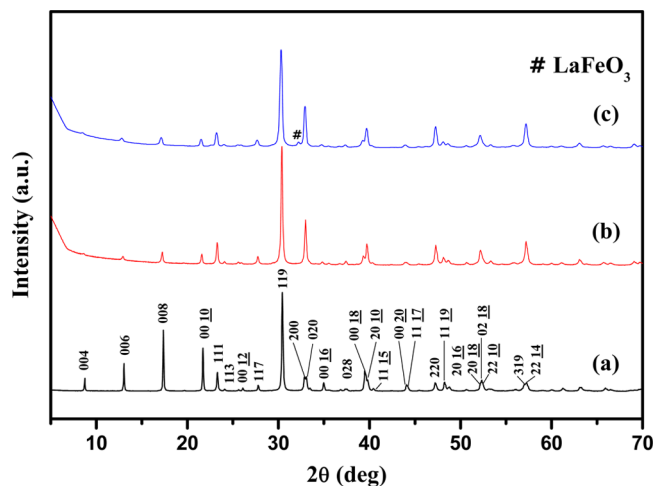

Figure 2. PXD patterns of (a) Bi$_5$Ti$_3$FeO$_{15}$, (b) Bi$_4$LaTi$_3$FeO$_{15}$, and (c) Bi$_3$La$_2$Ti$_3$FeO$_{15}$.

standard JCPDS data of the parent Bi$_5$Ti$_3$FeO$_{15}$ (JCPDS PDF # 89−8545) indicated formation of pure phase four layer Aurivillius perovskites, excepting for Bi$_3$La$_2$Ti$_3$FeO$_{15}$, where a small impurity of LaFeO$_3$ was detected. All the peaks observed in the PXD pattern of Bi$_4$LaTi$_3$FeO$_{15}$ are indexable in the orthorhombic $A2_1am$ space group.[32] In case of Bi$_3$La$_2$Ti$_3$FeO$_{15}$, all the diffraction peaks except those assigned to LaFeO$_3$ (Figure 2c) are indexable in the same $A2_1am$ space group. The least-squares refined lattice parameters for the compounds are given in Table 1. The lattice parameters for the parent Bi$_5$Ti$_3$FeO$_{15}$ are in good agreement with the literature data.[32]

Table 1. Lattice Parameters and Band Gap of Bi$_{5-x}$La$_x$Ti$_3$FeO$_{15}$ ($x = 0−2$)

	lattice parameters (Å)			band gap (eV)	
compd	a	b	c	E_g (1)	E_g (2)
Bi$_5$Ti$_3$FeO$_{15}$	5.458(3)	5.421(3)	41.02(2)	2.09	2.62
Bi$_4$LaTi$_3$FeO$_{15}$	5.436(1)	5.420(2)	41.19(1)	2.08	2.67
Bi$_3$La$_2$Ti$_3$FeO$_{15}$	5.437(1)	5.436(1)	41.29(1)	2.01	2.71

A closer look at the lattice parameters (Table 1) of Bi$_{5-x}$La$_x$Ti$_3$FeO$_{15}$ series shows a slight increase in the c-parameter as x varies from 0−2, while a and b-parameter approach each other and become nearly equal in Bi$_3$La$_2$Ti$_3$FeO$_{15}$. This clearly indicates a decrease in orthorhombic distortion and a shift toward tetragonal structure with progressive replacement of lone-pair active Bi^{3+} by La^{3+} (having no lone-pair of electrons). It is reported that the La-incorporation in the perovskite A-site diminishes the out-of-center distortion,[38] which possibly leads to an increase in the c-parameter of the compounds with increasing La-substitution. The PXD simulation studies on Bi$_3$La$_2$Ti$_3$FeO$_{15}$ indicated La-

substitution at the $[Bi_2O_2]^{2+}$ layers. The simulation result also showed preferential occupation ($\sim$67−75%) of La in A-site of the central perovskite layer and the residual Bi and La, apart from those occupied central perovskite and $[Bi_2O_2]^{2+}$ layers, were located in the terminal perovskite layers. The positional parameters, occupancy and thermal factors used in the PXD pattern simulation are shown in Table S1 in the Supporting Information and the simulated pattern is compared with the observed data in Figure S1 in the Supporting Information. Now, as shown in Figure 1, due to intergrowth nature of the Aurivillius phases by alternate layering of fluorite-type $[Bi_2O_2]^{2+}$ and $[A_{n-1}B_nO_{3n+1}]^{2-}$ perovskite sheets, a mismatch in the in-plane lattice parameters of the units would induce a strain in the structure. Moreover, changes in the Bi/La distribution over the $[Bi_2O_2]$ layer and A-site of the perovskite blocks would give rise to subtle changes in the in-plane lattice parameter as well. Therefore, the Bi/La cation disorder takes place in such a way that this mismatch strain is reduced and an Aurivillius phase is stabilized. A cation disorder mediated relief of mismatch strain is attributed for monoclinic to orthorhombic structural transition in $Bi_{4-x}La_xTi_3O_{12}$.[39] The trend of lattice parameter variation and cation distribution observed in $Bi_{5-x}La_xTi_3FeO_{15}$ series are similar to those observed in La-substituted $Bi_{4-x}La_xTi_3O_{12}$ with increase in La^{3+} substitution. We were not been able to synthesize $Bi_2La_3Ti_3FeO_{15}$ ($x = 3$) member of the general composition $Bi_{5-x}La_xTi_3FeO_{15}$). The destabilization of the Aurivillius phase, $Bi_2La_3Ti_3FeO_{15}$, could probably be due to an expected large mismatch strain that would have resulted by the larger amount of La present in the composition, thereby giving only a mixed phase with large quantities of $LaFeO_3$ impurity.

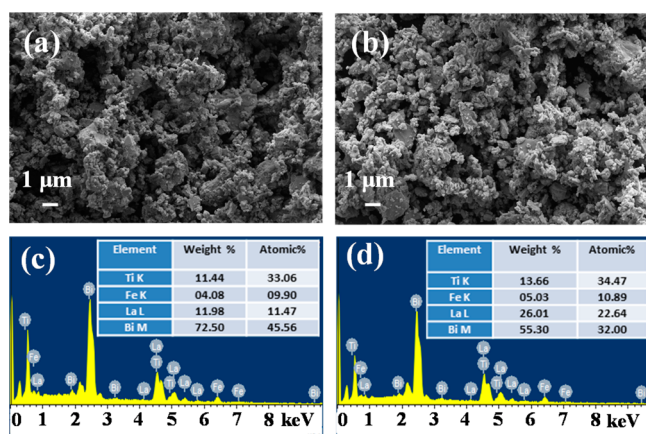**FE-SEM and EDS Analysis.** FE-SEM images of $Bi_{5-x}La_xTi_3FeO_{15}$ ($x = 1, 2$) are shown in Figure 3. The

Figure 3. FE-SEM images of (a) $Bi_4LaTi_3FeO_{15}$ and (b) $Bi_3La_2Ti_3FeO_{15}$. Corresponding EDS analyses are shown in c and d.

images show homogeneous morphology over the entire region of imaging with plate-like crystallites having a quite large variation in their sizes ranging from few hundred nanometers to few micrometers. Moreover, there appears to be fairly large degree of agglomeration among the crystallites. Elemental ratios as obtained from EDS analyses, both on spot and area basis, were in excellent agreement with the nominal compositions.

FE-SEM-EDS Elemental Mapping Analysis. To analyze the elemental distribution in $Bi_{5-x}La_xTi_3FeO_{15}$ ($x = 1, 2$) compounds, EDS elemental mapping was conducted. The

mapping shows (Figure 4) uniform distribution of all elements throughout the selected area of FE-SEM image. It clearly shows that the amount of La has increased and that of Bi has decreased in going from $Bi_4LaTi_3FeO_{15}$ to $Bi_3La_2Ti_3FeO_{15}$ while the amount of Ti and Fe remained largely unchanged as expected for the nominal compositions. The bright spot observed in Figure 3h could probably be due to the impurity phase $LaFeO_3$ showing accumulation of Fe (Figure 4h).

UV−Vis DRS Analysis. The UV−vis DRS (Figure 5) for all the compounds show absorption edges in the visible region ($\lambda > 400$ nm). Assuming $Bi_4LaTi_3FeO_{15}$ and $Bi_3La_2Ti_3FeO_{15}$ to be indirect band gap semiconductors, like $Bi_5Ti_3FeO_{15}$,[40] band gap energies (E_g) were estimated from the plot of $(\alpha h\nu)^{1/2}$ versus $h\nu$ (Figure 5b). The E_g for the compounds are given in Table 1. Two absorption edges could be observed in $Bi_{5-x}La_xTi_3FeO_{15}$ (Figure 5a); the first band is ascribed to the transition from the hybridized O 2p + Bi 6s + Fe t_{2g} valence band (VB) states to Fe e_g conduction band (CB) states with corresponding band gap E_g (1) and the other from the same VB to Ti 3d CB states with corresponding band gap E_g (2). The interband transitions are shown schematically in the inset of Figure 5a.[15] Because all the compounds reported here are visible light absorber with band gaps ranging from $\sim$2.0 to 2.7 eV, it suggested their potential use in visible-light-driven photocatalysis.

PL Analysis. PL spectra of $Bi_{5-x}La_xTi_3FeO_{15}$ ($x = 0−2$) were recorded with an excitation wavelength of 350 nm. All the compounds show broad emission spectra (410−580 nm) with a peak around 470 nm (Figure 6). Because the PL intensity is an indicator of electron−hole recombination rate, a lower PL intensity indicates slow recombination, therefore, longer lifetime of electron−hole pairs.[41] This would suggest a higher efficiency of photocatalytic dye degradation for the catalyst having lower PL intensity. On the basis of the PL data (Figure 6), one would expect lowest photocatalytic activity for $Bi_4LaTi_3FeO_{15}$, if all other factors are considered to remain fixed. To our surprise, we observed highest degradation rate for $Bi_4LaTi_3FeO_{15}$ (see the Photocatalytic Activity section). This suggests that other factors such as adsorption of the dye on the catalyst surface, the position of valence and conduction band edges of the catalyst and the relative positioning of the HOMO−LUMO states of the dye must be responsible for enhanced activity.

Sun-Light-Driven Photocatalytic Activity. The photocatalytic activity of the compounds was evaluated by RhB degradation under natural sun light at various pH (2, 3, 7, and 11). Enhanced photocatalytic degradation of RhB was observed over all the catalyst systems at pH 2. The RhB was degraded almost completely within 25−40 min of solar illumination (Figure 7a). Our results have been compared with blank runs under same pH and solar illumination without catalysts to show photostability (no self-degradation) of the dye.

The kinetics of the photocatalytic RhB degradation over $Bi_{5-x}La_xTi_3FeO_{15}$ ($x = 0−2$) catalysts was investigated based on Langmuir−Hinshelwood model[42]

$$\ln(C_0/C) = kt \tag{5}$$

where C_0 is the initial dye concentration, C is the dye concentration at time t and k is the pseudo-first-order rate constant. The linear plot between $\ln(C_0/C)$ and irradiation time (t) for $Bi_{5-x}La_xTi_3FeO_{15}$ ($x = 0−2$) compounds indicated the photocatalytic RhB degradation to follow a first-order kinetics. The degradation rate constants (k) are calculated from the slope of $\ln(C_0/C)$ versus t plot. Among all the compounds,
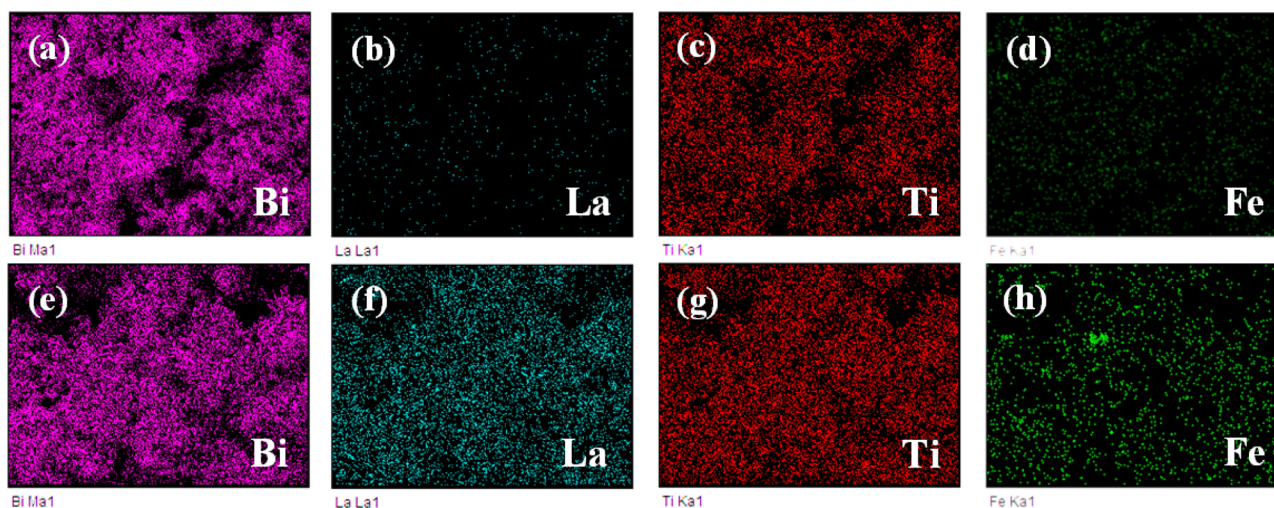
Figure 4. EDS elemental mapping of (a) Bi, (b) La, (c) Ti, and (d) Fe in $Bi_4LaTi_3FeO_{15}$, and (e−h) elemental mapping for $Bi_3La_2Ti_3FeO_{15}$ in the same order.

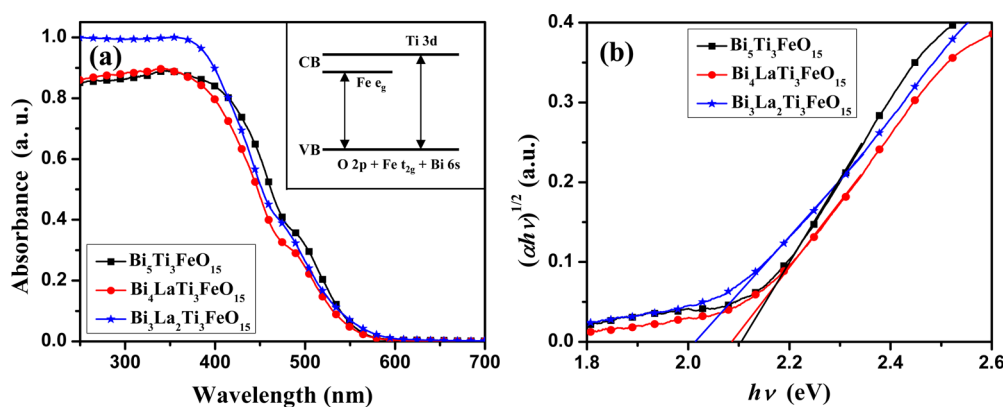**Figure 5.** (a) UV−vis diffuse reflectance spectra (DRS). A schematic diagram showing interband transitions in $Bi_{5−x}La_xTi_3FeO_{15}$ ($x = 0−2$) is shown in the inset. (b) Kubelka−Munk plot for the calculation of band gap of $Bi_{5−x}La_xTi_3FeO_{15}$ ($x = 0−2$).
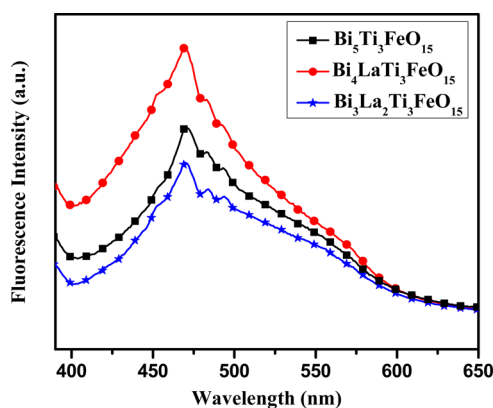

Figure 6. Photoluminescence spectra of $Bi_{5−x}La_xTi_3FeO_{15}$ ($x = 0−2$) at room temperature (excitation at 350 nm).

$Bi_4LaTi_3FeO_{15}$ shows the best degradation rate constant (Figure 7b) and follows the order; $Bi_4LaTi_3FeO_{15}$ ($k = 0.18853$ min^{-1}) > $Bi_3La_2Ti_3FeO_{15}$ ($k = 0.13143$ min^{-1}) > $Bi_5Ti_3FeO_{15}$ ($k = 0.11002$ min^{-1}).

Degradation studies at pH 3 also showed near complete degradation of the dye molecule but required longer illumination time ranging from 30 to 90 min (see Figure S2 in the Supporting Information). However, the degradation studies at higher pH such as, 7 and 11 did not show any appreciable degradation of the dye indicating almost no photocatalysis.

The RhB degradation at pH 2 was further confirmed by measuring the chemical oxygen demand (COD) of RhB solution which decreased by 94−99% within 30−60 min of solar illumination depending on the catalysts used (see Figure S3 in the Supporting Information).

Catalyst Stability and Photocatalytic Cycle Studies. To evaluate the stability and reusability of the photocatalysts, the RhB degradation process was repeated for five cycles (see Experimental Section). Figure 8 shows a typical UV−vis absorption data of RhB over $Bi_4LaTi_3FeO_{15}$ along with the degradation profiles for five successive catalytic cycles. In every cycle ∼99% of RhB were degraded within 25 min of sun-light irradiation with complete decolorization of the dye solution, indicating no observable loss of activity of the catalyst (Figure 8b). The dye degradation profiles for $Bi_3La_2Ti_3FeO_{15}$ and parent $Bi_5Ti_3FeO_{15}$ over five catalytic cycles are given in the Supporting Information (Figure S4). The PXD patterns recorded for all the catalysts recovered after the fifth cycle of photocatalysis run are shown in Figure 9. The PXD data did not show any impurity due to decomposition or phase separation, indicating no photocorrosion or photoleaching during dye degradation. Moreover, the crystallinity of the
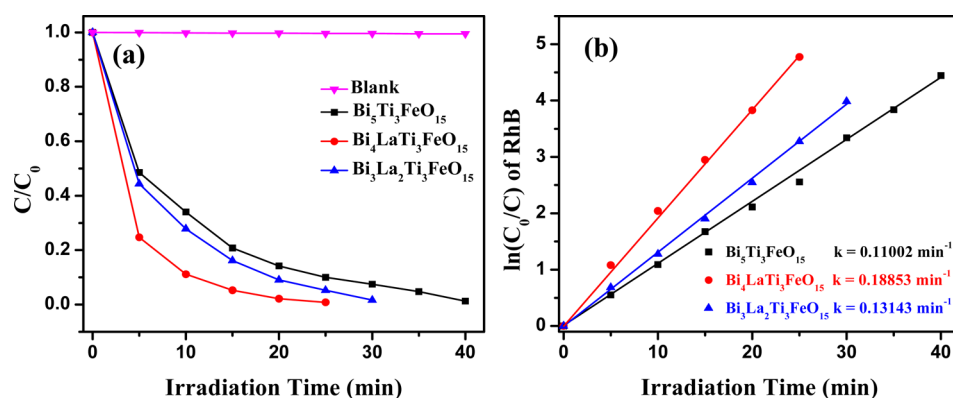
Figure 7. (a) Photocatalytic degradation of RhB with time by $Bi_{5-x}La_xTi_3FeO_{15}$ ($x = 0-2$) under sun-light. (b) Plot of $\ln(C_0/C)$ as a function of time over $Bi_{5-x}La_xTi_3FeO_{15}$ ($x = 0-2$).
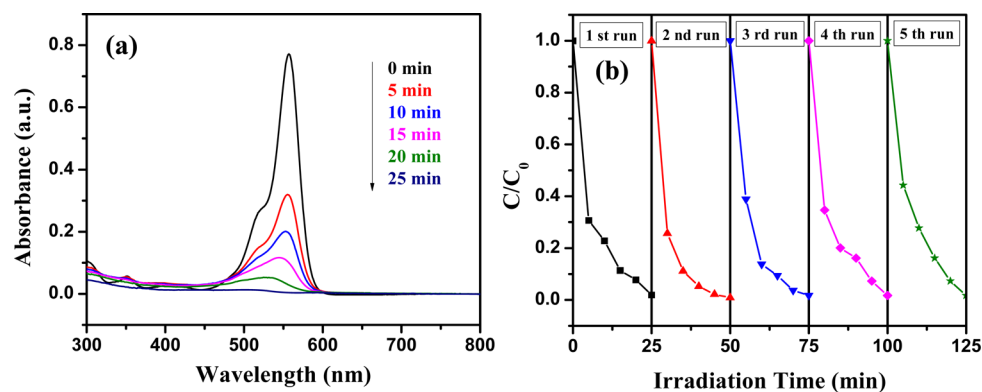

Figure 8. (a) UV–vis absorption spectra of RhB as a function of irradiation time for $Bi_4LaTi_3FeO_{15}$. (b) Time profiles of RhB degradation for five successive cycles with $Bi_4LaTi_3FeO_{15}$ under sun-light irradiation.

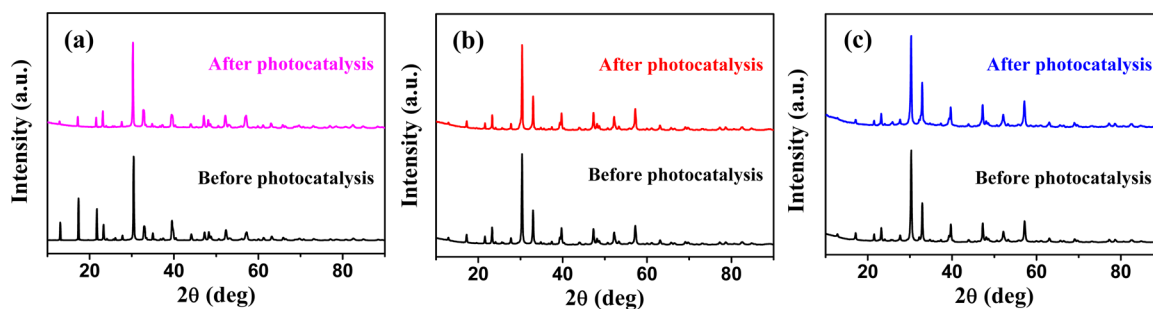**Figure 9.** PXD patterns of (a) $Bi_5Ti_3FeO_{15}$, (b) $Bi_4LaTi_3FeO_{15}$, and (c) $Bi_3La_2Ti_3FeO_{15}$ before and after the photocatalytic RhB degradation.

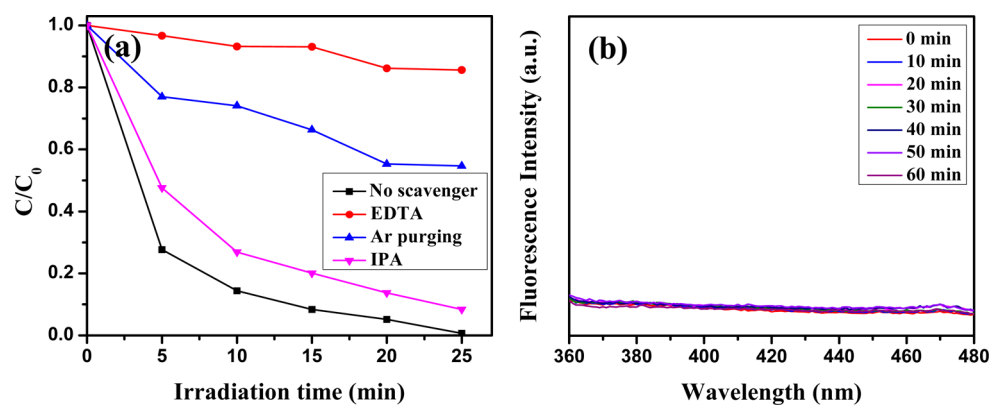**Figure 10.** (a) Effects of different scavengers on the degradation of RhB in the presence of $Bi_4LaTi_3FeO_{15}$ catalyst under sun-light irradiation. (b) •OH trapping PL spectra of $Bi_4LaTi_3FeO_{15}$ compound in a basic solution of TA (excitation at 315 nm).

postdegradation catalysts was almost retained showing excellent stability and robustness of the catalysts under the reaction condition.

Detection of Reactive Species. The radical and hole trapping experiments (scavenger tests) with different scavenger molecules were carried out to elucidate the photocatalytic degradation mechanism of RhB under sun-light irradiation over $Bi_4LaTi_3FeO_{15}$. Generally, the reactive species such as, hydroxyl radicals ($^\bullet OH$), superoxide radical anions ($O_2^{\bullet -}$) and holes (h^+) are expected to be involved in the photocatalytic dye degradation processes.[43] The photocatalytic activity of RhB is drastically suppressed in a controlled experiment when EDTA was used as a hole scavenger (Figure 10). Moreover, when Argon purging was conducted during degradation, the RhB degradation is inhibited (Figure 10) to a moderate extent. However, no significant change in the degradation of RhB is observed upon the addition of IPA as a $^\bullet OH$ scavenger as compared to uncontrolled experiments without scavengers under similar conditions. This indicates that h^+ and $O_2^{\bullet -}$ are playing a dominant role in the photocatalytic degradation of RhB over $Bi_4LaTi_3FeO_{15}$ under sun-light.

Moreover, the PL spectra did not show any indication of $^\bullet OH$ generation, when terephthalic acid (TA) was used as a probe molecule,[44] which readily reacts with $^\bullet OH$ to produce highly fluorescent 2-hydroxyterephthelic acid (HTA) having a λ_{max} at ~425 nm. The absence of a PL emission peak for HTA at ~425 nm (Figure 10b) indicated no $^\bullet OH$ formation with time. This, however, confirmed that $^\bullet OH$ does not play any role in the photodegradation of RhB with $Bi_4LaTi_3FeO_{15}$ under the reaction condition reported here.

Mechanistic Insights for Enhanced Photocatalytic Activity. The semiconductor photocatalysis with dyes is known largely to occur through dye adsorption on the surface of the photocatalyst, followed by e^-–h^+ generation on photoexcitation and oxidative breakdown of the dye molecule on action of reactive species generated. To investigate further into the degradation process and to find out the reason for high activity of the catalyst, we have looked into the energy level alignment of the photocatalyst with respect to the potential of $^\bullet OH/H_2O$, $O_2/O_2^{\bullet -}$ and HOMO–LUMO levels of RhB. The conduction band edge minima (E_{CB}) and valence band maxima (E_{VB}) of the semiconductor photocatalysts were calculated empirically using the following expressions[45]

$$E_{CB} = \chi(A_aB_bC_c) - \frac{1}{2}E_g + E_0 \tag{6}$$

$$E_{VB} = E_{CB} + E_g \tag{7}$$

where E_g is the band gap of the semiconductor, E_{CB} is the conduction band potential, E_{VB} is the valence band potential, E_0 is the scale factor taken as -4.5 eV with respect to normal hydrogen electrode (NHE scale) and $\chi(A_aB_bC_c)$ is the absolute electronegativity (AE) of the semiconductor $A_aB_bC_c$. The AE of a compound semiconductor is calculated as the geometric mean of the AE of the constituent atoms. For our calculation, the AE values for Bi, La, Ti, Fe, and O are taken as 4.69, 3.1, 3.45, 4.06, and 7.54, respectively.[46] The calculated values of valence and conduction band positions of $Bi_{5-x}La_xTi_3FeO_{15}$ ($x = 0-2$) are given in Table 2. The potential of $^\bullet OH/H_2O$ ($+ 2.68$ eV vs. NHE), $O_2/O_2^{\bullet -}$ ($+ 0.13$ eV vs. NHE) and HOMO–LUMO levels of RhB ($E_{HOMO} = 0.95$ eV and $E_{LUMO} = -1.42$ eV that matches fairly well with the λ_{max} of 553 nm) were taken from the literature.[43,47] Figure 11 shows the energy level diagram of

Table 2. Calculated Values of Valence and Conduction Band Positions of $Bi_{5-x}La_xTi_3FeO_{15}$ ($x = 0-2$)

compd	valence band (eV)	conduction band-1 (eV)	conduction band-2 (eV)
$Bi_5Ti_3FeO_{15}$	2.58	0.49	-0.04
$Bi_4LaTi_3FeO_{15}$	2.47	0.39	-0.20
$Bi_3La_2Ti_3FeO_{15}$	2.34	0.33	-0.37

$Bi_4LaTi_3FeO_{15}$ with respect to the potential of $^\bullet OH/H_2O$, $O_2/O_2^{\bullet -}$, and HOMO–LUMO levels of RhB.
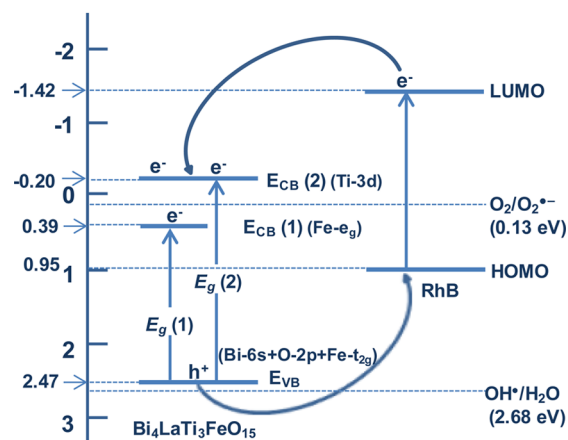
Figure 11. Schematic energy level diagram of $Bi_4LaTi_3FeO_{15}$ with respect to potential (vs NHE) of $^\bullet OH/H_2O$, $O_2/O_2^{\bullet -}$, and the HOMO–LUMO levels of RhB.

It is evident from the UV–vis DRS of the semiconductors and according to earlier discussions, there exists two CB edges (one primarily of Ti 3d character and the other Fe e_g character) and a VB edge (hybridized states of O 2p + Bi 6s + Fe t_{2g}). Apparently, this would give rise to two absorption edges arising out of the transitions from the VB to both the CBs as shown in Figure 5. These two transitions correspond to the band gap energies of 2.08 and 2.67 eV for $Bi_4LaTi_3FeO_{15}$. It is clear from the potential vs NHE energy level diagram that the position of E_{VB} above the potential of $^\bullet OH/H_2O$ is not suitable for $^\bullet OH$ formation. Similarly, the position of E_{CB} (1) below the potential of $O_2/O_2^{\bullet -}$ is not in favor of $O_2^{\bullet -}$ generation. However, the position of E_{CB} (2), which lies above the potential of $O_2/O_2^{\bullet -}$, is suitable for the $O_2^{\bullet -}$ formation. Although, the passage of electron from E_{CB} (2) to E_{CB} (1), an alternate and competing pathway for electron transfer, would diminish the probability of $O_2^{\bullet -}$ formation. Since both the electronic states are part of the same single-phase semiconductor photocatalyst, the e^- transfer from E_{CB} (2) to E_{CB} (1) will be at ease. The above facts explain the results of Argon purging test, to show a moderate role of $O_2^{\bullet -}$ and the IPA scavenger test, to signify only a marginal or no role of $^\bullet OH$ in the RhB degradation. The later was further confirmed by the PL studies (Figure 10b). Moreover, the positioning of E_{VB} below the HOMO levels of RhB in the energy level diagram is suitable for h^+ transfer from semiconductor to adsorbed dye molecules and supportive for the role of h^+ in RhB degradation. The drastic decrease in degradation rate in the presence of an h^+ scavenger (EDTA) further confirmed that the RhB degradation over $Bi_4LaTi_3FeO_{15}$ was largely mediated by holes. On the basis of

our experimental results, a plausible mechanism for the photocatalytic RhB degradation over $Bi_4LaTi_3FeO_{15}$ catalyst under sun-light irradiation is shown in Figure 12.
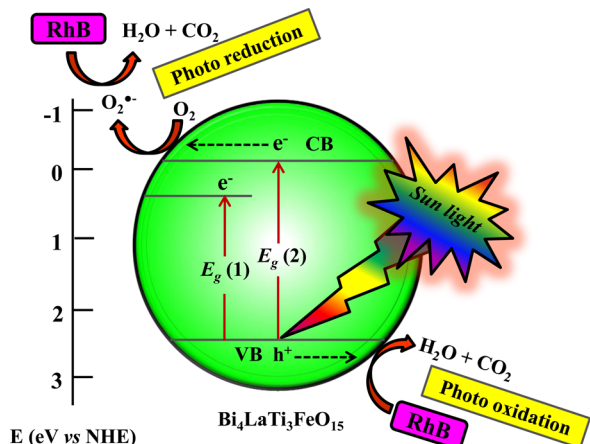

Figure 12. Schematic diagram showing the photocatalytic RhB degradation over $Bi_4LaTi_3FeO_{15}$ catalyst under sun-light irradiation.

1. Role of Adsorption. It is believed that for h^+-mediated dye degradation, the attachment of the dye molecule with the catalyst surface plays an important role. To elucidate the role of dye adsorption on the photocatalytic activity, we have performed adsorption experiments on dye-catalyst suspensions at different pH in the dark (see the Experimental Section). Interestingly, the adsorption data indicates that nearly 50% of dye molecules are adsorbed on the surface of $Bi_4LaTi_3FeO_{15}$ at pH 2 and a marked decrease in adsorption in neutral and alkaline pH (see Figure S5 in the Supporting Information). The corresponding adsorption data for $Bi_5Ti_3FeO_{15}$ and $Bi_3La_2Ti_3FeO_{15}$ are 37 and 47%, respectively, at pH 2 and a similar decrease is observed in neutral and alkaline medium. This indeed, explains the enhanced activity of the catalyst in acidic pH and very poor performance in neutral and alkaline pH. Moreover, the activity of the catalysts follows the adsorption order making $Bi_4LaTi_3FeO_{15}$ as the most active and decreases in the order $Bi_4LaTi_3FeO_{15} > Bi_3La_2Ti_3FeO_{15} > Bi_5Ti_3FeO_{15}$ (Figure 7).

2. Role of ζ-Potential. The ζ-potential of the catalysts plays important role in the adsorption process. The surface charge of the photocatalysts is determined by measuring the ζ-potential. Figure 13 shows the variation of ζ-potential for $Bi_{5-x}La_xTi_3FeO_{15}$ ($x = 0-2$) catalysts as a function of pH. The highest positive ζ-potentials are seen at pH 2. As the pH increases, the ζ-potential shows a decreasing trend from more positive to less positive and finally to negative potentials in the alkaline pH. This is largely due to the action of H^+ and OH^- ions on the surface hydroxyl groups of the semiconductor.

It is interesting to note that the biggest adsorption of RhB took place in case of $Bi_4LaTi_3FeO_{15}$, which had the highest ζ-

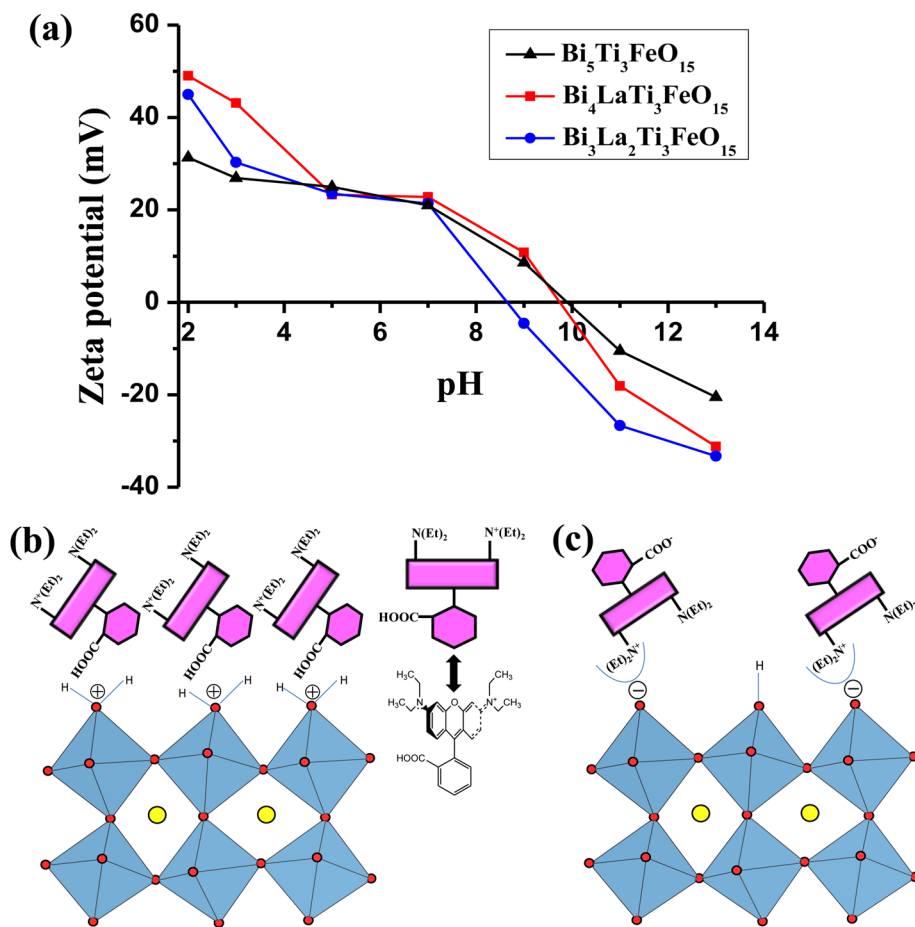**Figure 13.** (a) ζ-potential of $Bi_{5-x}La_xTi_3FeO_{15}$ ($x = 0-2$) catalysts at different pH. Adsorption schemes of RhB on the catalyst surface at (b) acidic (pH 2) and (c) alkaline (pH 11) mediums.

potential (+ 49.1 mV) among all the members, $Bi_{5-x}La_xTi_3FeO_{15}$, at pH 2. The ζ-potentials for $Bi_3La_2Ti_3FeO_{15}$ and $Bi_5Ti_3FeO_{15}$ were +45.0 and +31.3 mV, respectively, at pH 2. Indeed, the value of ζ-potential was reflected in the adsorption data for $Bi_3La_2Ti_3FeO_{15}$ and $Bi_5Ti_3FeO_{15}$ being the highest at pH 2 and then a decrease in adsorption with decreasing positive ζ- potential.

The adsorption of RhB under acidic pH may be explained on the basis of a schematic diagram (Figure 13), where the positive charge generated on the catalyst surface can effectively accommodate RhB molecules through electrostatic interaction with carboxylic acid groups of the dye molecule. At higher pH (pH 11), the catalyst surface acquires a negative charge and the carboxylate anionic group of the RhB would be repelled. However, the RhB molecule can get adsorbed on the negatively charged surface through electrostatic interaction with the positively charged N-diethyl end. But, the steric bulkiness of the N-diethyl group would not allow effective adsorption of RhB. Moreover, the magnitude of negative ζ- potential (−10 to −31 mV) is significantly lower as compared to that of positive potential at pH 2. These above two factors, in fact, would reduce the extent of dye adsorption considerably. This observation led us to believe that a different mode together with a very low amount of dye adsorption is responsible for nearly zero photocatalytic RhB degradation in the alkaline medium.

Lastly, considering the possible ferroelectric nature of the compounds,[26,27] ($Bi_4LaTi_3FeO_{15}$ and $Bi_3La_2Ti_3FeO_{15}$ also crystallizes in the noncentrosymmetric space group, $A2_1am$) the internal electric fields from ferroelectric domains and surface polarizations might be playing important role for enhanced dye adsorption and concomitant high photocatalytic activity of these catalysts. Enhanced photocatalytic activity of ferroelectric oxides has been accounted in the recent literature.[48,49] Moreover, the internal electric fields of the semiconductor catalysts might also be helping in efficient charge carrier separation,[50] which in turn would enhance the photocatalytic dye degradation. Further work is required to fully understand the precise role of ferroelectric domains and charge polarization on adsorption, zeta potential, and photocatalytic activity in these layered Aurivillius perovskites.

CONCLUSIONS

A highly efficient sun-light driven RhB degradation by a series of Aurivillius layered perovskites, $Bi_{5-x}La_xTi_3FeO_{15}$ ($x = 0-2$), in aqueous acidic solution has been demonstrated. The compounds, $Bi_4LaTi_3FeO_{15}$ and $Bi_3La_2Ti_3FeO_{15}$ were synthesized for the first time in the bulk form by solid state reaction. The activity of the catalysts toward RhB degradation is comparable or higher than many of the single-phase and composite catalysts with Aurivillius and perovskite structures in the bulk or nanostructured form reported recently. An enhanced charge separation rendering slow $e^-–h^+$ recombination and efficient transport of photogenerated holes could possibly be the rationale for high efficiency of the bulk catalysts irrespective of the degradation mechanisms involved. Moreover, the large positive ζ-potential led to enhanced dye adsorption and consequently a high rate of degradation. Scavenger test experiments clearly indicated the dominant role of holes in the degradation process involving the Aurivillius layered oxides reported here. The positioning of VB and CB edges with respect to potentials of $^\bullet OH/H_2O$, $O_2/O_2^{\bullet-}$, and HOMO−LUMO levels of RhB clearly corroborated with the scavenger test results indicating no major role of hydroxyl species in the degradation. Considering the effect of ferroelectricity for enhanced photocatalytic activity in the recent literature, the role of internal electric fields and surface polarizations of these polar Aurivillius oxides for enhanced dye adsorption and photocatalytic activity may not be ruled out. Lastly, due to their high activity, these compounds may find practical applications in the area of organic contaminant detoxification, indoor air purification (VOC control), photocurrent generation and hydrogen production by water-splitting reaction, all under sun-light irradiation.

ASSOCIATED CONTENT

⑤ Supporting Information
Table S1: Atomic position, site occupancy and thermal parameters used for PXD simulation of $Bi_3La_2Ti_3FeO_{15}$. Figure S1: Observed and simulated PXD patterns of $Bi_3La_2Ti_3FeO_{15}$. Figure S2: UV−vis absorption spectral changes of the aqueous RhB solutions over $Bi_{5-x}La_xTi_3FeO_{15}$ ($x = 0-2$). Figure S2 also shows the course of photodegradation at different pH for $Bi_{5-x}La_xTi_3FeO_{15}$ ($x = 0-2$). Figure S3: COD removal efficiency of $Bi_{5-x}La_xTi_3FeO_{15}$ ($x = 0-2$) with time. Figure S4: Time profiles of RhB degradation over five successive cycles for $Bi_5Ti_3FeO_{15}$ and $Bi_3La_2Ti_3FeO_{15}$ under sun-light irradiation. Figure S5: Influence of pH on RhB adsorption onto $Bi_{5-x}La_xTi_3FeO_{15}$ ($x = 0-2$) catalyst surfaces. This material is available free of charge via the Internet at http://pubs.acs.org.

AUTHOR INFORMATION

Corresponding Author
*E-mail: tapasfcy@iitr.ac.in. Fax: 91-1332-273560. Tel.: 91-1332-285864.

Notes
The authors declare no competing financial interest.

ACKNOWLEDGMENTS

ABBREVIATIONS

AE, absolute electronegativity
COD, chemical oxygen demand
CB, conduction band
HTA, hydroxy terephthalic acid
IPA, isopropyl alcohol
RhB, rhodamine B
TA, terephthalic acid
VB, valence band

REFERENCES

(1) Hoffmann, M. R.; Martin, S. T.; Choi, W.; Bahnemann, D. W. Environmental Applications of Semiconductor Photocatalysis. *Chem. Rev.* **1995**, *95*, 69−96.
(2) Chen, X.; Shen, S.; Guo, L.; Mao, S. S. Semiconductor-Based Photocatalytic Hydrogen Generation. *Chem. Rev.* **2010**, *110*, 6503−6570.
(3) Osterloh, F. E. Inorganic Materials as Catalysts for Photochemical Splitting of Water. *Chem. Mater.* **2008**, *20*, 35−54.
(4) Kudo, A.; Miseki, Y. Heterogeneous Photocatalyst Materials for Water Splitting. *Chem. Soc. Rev.* **2009**, *38*, 253−278.

(5) Tang, J.; Zou, Z.; Ye, J. Efficient Photocatalytic Decomposition of Organic Contaminants over CaBi$_2$O$_4$ under Visible-Light Irradiation. *Angew. Chem., Int. Ed.* **2004**, *43*, 4463−4466.

(6) Kim, H. G.; Hwang, D. W.; Lee, J. S. An Undoped, Single-Phase Oxide Photocatalyst Working under Visible Light. *J. Am. Chem. Soc.* **2004**, *126*, 8912−8913.

(7) Wang, D.; Kako, T.; Ye, J. Efficient Photocatalytic Decomposition of Acetaldehyde over a Solid-Solution Perovskite (Ag$_{0.75}$Sr$_{0.25}$)-(Nb$_{0.75}$Ti$_{0.25}$)O$_3$ under Visible-Light Irradiation. *J. Am. Chem. Soc.* **2008**, *130*, 2724−2725.

(8) Kim, H. G.; Borse, P. H.; Jang, J. S.; Ahn, C. W.; Jeong, E. D.; Lee, J. S. Engineered Nanorod Perovskite Film Photocatalysts to Harvest Visible Light. *Adv. Mater.* **2011**, *23*, 2088−2092.

(9) Colón, G.; López, S. M.; Hidalgo, M. C.; Navío, J. A. Sunlight Highly Photoactive Bi$_2$WO$_6$−TiO$_2$ Heterostructures for Rhodamine B Degradation. *Chem. Commun.* **2010**, *46*, 4809−4811.

(10) Kudo, A.; Omori, K.; Kato, H. A Novel Aqueous Process for Preparation of Crystal Form-Controlled and Highly Crystalline BiVO$_4$ Powder from Layered Vanadates at Room Temperature and Its Photocatalytic and Photophysical Properties. *J. Am. Chem. Soc.* **1999**, *121*, 11459−11467.

(11) Tokunaga, S.; Kato, H.; Kudo, A. Selective Preparation of Monoclinic and Tetragonal BiVO$_4$ with Scheelite Structure and Their Photocatalytic Properties. *Chem. Mater.* **2001**, *13*, 4624−4628.

(12) Tang, J.; Zou, Z.; Ye, J. Photocatalytic Decomposition of Organic Contaminants by Bi$_2$WO$_6$ under Visible Light Irradiation. *Catal. Lett.* **2004**, *92*, 53−56.

(13) Muktha, B.; Priya, M. H.; Madras, G.; Guru Row, T. N. Synthesis, Structure, and Photocatalysis in a New Structural Variant of the Aurivillius Phase: LiBi$_4$M$_3$O$_{14}$ (M = Nb, Ta). *J. Phys. Chem. B* **2005**, *109*, 11442−11449.

(14) Fu, H.; Pan, C.; Yao, W.; Zhu, Y. Visible-Light-Induced Degradation of Rhodamine B by Nanosized Bi$_2$WO$_6$. *J. Phys. Chem. B* **2005**, *109*, 22432−22439.

(15) Sun, S.; Wang, W.; Xu, H.; Zhou, L.; Shang, M.; Zhang, L. Bi$_5$FeTi$_3$O$_{15}$ Hierarchical Microflowers: Hydrothermal Synthesis, Growth Mechanism, and Associated Visible-Light-Driven Photocatalysis. *J. Phys. Chem. C* **2008**, *112*, 17835−17843.

(16) Yu, K.; Yang, S.; He, H.; Sun, C.; Gu, C.; Ju, Y. Visible Light-Driven Photocatalytic Degradation of Rhodamine B over NaBiO$_3$: Pathways and Mechanism. *J. Phys. Chem. A* **2009**, *113*, 10024−10032.

(17) Jang, J. S.; Yoon, S. S.; Borse, P. H.; Lim, K. T.; Hong, T. E.; Jeong, E. D.; Jung, O.-S.; Shim, Y. B.; Kim, H. G. Synthesis and Characterization of Aurivillius Phase Bi$_5$Ti$_3$FeO$_{15}$ Layered Perovskite for Visible Light Photocatalysis. *J. Cer. Soc. Jpn.* **2009**, *117*, 1268−1272.

(18) Mann, A. K. P.; Steinmiller, E. M. P.; Skrabalak, S. E. Elucidating the Structure-Dependent Photocatalytic Properties of Bi$_2$WO$_6$: A Synthesis Guided Investigation. *Dalton Trans.* **2012**, *41*, 7939−7945.

(19) Oshikiri, M.; Boero, M.; Ye, J.; Zou, Z.; Kido, G. Electronic Structures of Promising Photocatalysts InMO$_4$ (M = V, Nb, Ta) and BiVO$_4$ for Water Decomposition in the Visible Wavelength Region. *J. Chem. Phys.* **2002**, *117*, 7313−7318.

(20) Subbarao, E. C. Crystal Chemistry of Mixed Bismuth Oxides with Layer-Type Structures. *J. Am. Ceram. Soc.* **1962**, *45*, 166−169.

(21) Shimodaira, Y.; Kato, H.; Kobayashi, H.; Kudo, A. Photophysical Properties and Photocatalytic Activities of Bismuth Molybdates under Visible Light Irradiation. *J. Phys. Chem. B* **2006**, *110*, 17790−17797.

(22) Martínez-de la Cruz, A.; Alfaro, S. O.; Cuellar, E. L.; Méndez, U. O. Photocatalytic Properties of Bi$_2$MoO$_6$ Nanoparticles Prepared by an Amorphous Complex Precursor. *Catal. Today* **2007**, *129*, 194−199.

(23) Kudo, A.; Hijii, S. H$_2$ or O$_2$ Evolution from Aqueous Solution on Layered Oxide Photocatalysts Consisting of Bi^{3+} with 6s^2 Configuration and d^0 Transition Metal Ions. *Chem. Lett.* **1999**, *28*, 1103−1104.

(24) Zhang, L.; Man, Y.; Zhu, Y. Effects of Mo Replacement on the Structure and Visible-Light-Induced Photocatalytic Performances of Bi$_2$WO$_6$ Photocatalyst. *ACS Catal.* **2011**, *1*, 841−848.

(25) Zhou, L.; Yu, M.; Yang, J.; Wang, Y.; Yu, C. Nanosheet-Based Bi$_2$Mo$_x$W$_{1-x}$O$_6$ Solid Solutions with Adjustable Band Gaps and Enhanced Visible-Light-Driven Photocatalytic Activities. *J. Phys. Chem. C* **2010**, *114*, 18812−18818.

(26) Li, J.-B.; Huang, Y. P.; Rao, G. H.; Liu, G. Y.; Luo, J.; Chen, J. R.; Liang, J. K. Ferroelectric Transition of Aurivillius Compounds Bi$_5$Ti$_3$FeO$_{15}$ and Bi$_6$Ti$_3$Fe$_2$O$_{18}$. *Appl. Phys. Lett.* **2010**, *96*, 222903−222905.

(27) Nakashima, S.; Fujisawa, H.; Ichikawa, S.; Park, J. M.; Kanashima, T.; Okuyama, M.; Simizu, M. Structural and Ferroelectric Properties of Epitaxial Bi$_5$Ti$_3$FeO$_{15}$ and Natural-Superlattice-Structured Bi$_4$Ti$_3$O$_{12}$ − Bi$_5$Ti$_3$FeO$_{15}$ Thin Films. *J. Appl. Phys.* **2010**, *108*, 074106−074110.

(28) Porob, D. G.; Maggard, P. A. Synthesis of Textured Bi$_5$Ti$_3$FeO$_{15}$ and LaBi$_4$Ti$_3$FeO$_{15}$ Ferroelectric Layered Aurivillius Phases by Molten-Salt Flux Methods. *Mater. Res. Bull.* **2006**, *41*, 1513−1519.

(29) Morozov, M. I.; Gusarov, V. V. Synthesis of A$_{m-1}$Bi$_2$M$_m$O$_{3m+3}$ Compounds in the Bi$_4$Ti$_3$O$_{12}$−BiFeO$_3$ System. *Inorg. Mater.* **2002**, *38*, 723−729.

(30) Losocha, W.; Lewinski, K. PROSZKI- A System of Programs for Powder Diffraction Data Analysis. *J. Appl. Crystallogr.* **1994**, *27*, 437−438.

(31) Kraus, W.; Nolze, G. POWDER CELL - A Program for the Representation and Manipulation of Crystal Structures and Calculation of the Resulting X-ray Powder Patterns. *J. Appl. Crystallogr.* **1996**, *29*, 301−303.

(32) Hervoches, C. H.; Snedden, A.; Riggs, R.; Kilcoyne, S. H.; Manuel, P.; Lightfoot, P. Structural Behavior of the Four-Layer Aurivillius-Phase Ferroelectrics SrBi$_4$Ti$_4$O$_{15}$ and Bi$_5$Ti$_3$FeO$_{15}$. *J. Solid State Chem.* **2002**, *164*, 280−291.

(33) Kubelka, P.; Munk, F. Ein Beitrag zur Optik der Farbanstriche. *Z. Technol. Phys.* **1931**, *12*, 593−601.

(34) Tauc, J.; Grigorovic, R.; Vancu, A. Optical Properties and Electronic Structure of Amorphous Germanium. *Phys. Status Solidi* **1966**, *15*, 627−637.

(35) Kim, M. R.; Kang, Y.; Jang, D. Synthesis and Characterization of Highly Luminescent CdS@ZnS Core−Shell Nanorods. *J. Phys. Chem. C* **2007**, *111*, 18507−18511.

(36) Zhang, H.; Zong, R.; Zhao, J.; Zhu, Y. Dramatic Visible Photocatalytic Degradation Performances Due to Synergetic Effect of TiO$_2$ with PANI. *Environ. Sci. Technol.* **2008**, *42*, 3803−3807.

(37) Yang, H.; Li, G.; An, T.; Gao, Y.; Fu, J. Photocatalytic Degradation Kinetics and Mechanism of Environmental Pharmaceuticals in Aqueous Suspension of TiO$_2$: A Case of Sulfa Drugs. *Catal. Today* **2010**, *153*, 200−207.

(38) Halasyamani, P. S. Asymmetric Cation Coordination in Oxide Materials: Influence of Lone-Pair Cations on the Intra-Octahedral Distortion in d^0 Transition Metals. *Chem. Mater.* **2004**, *16*, 3586−3592.

(39) Chu, M.-W.; Caldes, M.-T.; Brohan, L.; Ganne, M.; Marie, A.-M.; Joubert, O.; Piffard, Y. Bulk and Surface Structures of the Aurivillius Phases: Bi$_{4-x}$La$_x$Ti$_3$O$_{12}$ (0 ≤ x ≤ 2.00). *Chem. Mater.* **2004**, *16*, 31−42.

(40) Wu, M.; Tian, Z.; Yuan, S.; Huang, Z. Magnetic and Optical Properties of the Aurivillius Phase Bi$_5$Ti$_3$FeO$_{15}$. *Mater. Lett.* **2012**, *68*, 190−192.

(41) Fujihara, K.; Izuni, S.; Ohno, S.; Matsumura, M. Time-resolved Photoluminescence of Particulate TiO2 Photocatalysts Suspended in Aqueous Solution. *J. Photochem. Photobiol., A* **2000**, *132*, 99−104.

(42) Fu, H.; Pan, C.; Yao, W.; Zhu, Y. Visible−Light−Induced Degradation of Rhodamine B by Nanosized Bi$_2$WO$_6$. *J. Phys. Chem. B* **2005**, *109*, 22432−22439.

(43) Kumar, S.; Surendar, T.; Baruah, A.; Shanker, V. Synthesis of a Novel and Stable g-C$_3$N$_4$−Ag$_3$PO$_4$ Hybrid Nanocomposite Photocatalyst and Study of the Photocatalytic Activity under Visible Light Irradiation. *J. Mater. Chem. A* **2013**, *1*, 5333−5340.

(44) Hirakawa, T.; Nosaka, Y. Properties of O$_2$$^{\bullet-}$ and OH$^\bullet$ Formed in TiO$_2$ Aqueous Suspensions by Photocatalytic Reaction and the Influence of H$_2$O$_2$ and some Ions. *Langmuir* **2002**, *18*, 3247−3254.

(45) Lv, J.; Kako, T.; Zou, Z.; Ye, J. Band Structure Design and Photocatalytic Activity of In_2O_3/N−$InNbO_4$ Composite. *Appl. Phys. Lett.* **2009**, *95*, 032107−032109.

(46) Pearson, R. G. Absolute Electronegativity and Hardness: Application to Inorganic Chemistry. *Inorg. Chem.* **1988**, *27*, 734−740.

(47) Pan, L.; Zou, J.; Liu, X.; Liu, X.; Wang, S.; Zhang, X.; Wang, L. Visible-Light-Induced Photodegradation of Rhodamine B over Hierarchical TiO_2: Effects of Storage Period and Water-Mediated Adsorption Switch. *Ind. Eng. Chem. Res.* **2012**, *51*, 12782−12786.

(48) Cui, Y.; Briscoe, J.; Dunn, S. Effect of Ferroelectricity on Solar-Light-Driven Photocatalytic Activity of $BaTiO_3$-Influence on the Carrier Separation and Stern Layer Formation. *Chem. Mater.* **2013**, *25*, 4215−4223.

(49) Li, L.; Salvador, P. A.; Rohrer, G. S. Photocatalysts with Internal Electric Fields. *Nanoscale* **2014**, *6*, 24−42.

(50) Grinberg, I.; West, D. V.; Torres, M.; Gou, G.; Stein, D. M.; Wu, L.; Chen, G.; Gallo, E. M.; Akbashev, A. R.; Davis, P. K.; Spanier, J. E.; Rappe, A. M. Perovskite Oxides for Visible-Light-Absorbing Ferro-electric and Photovoltaic Materials. *Nature* **2013**, *503*, 509−512.